



Influence of milling parameters on machining performances and surface quality of ZK61M magnesium alloy

Chenguang Wang¹ · Chang Chen¹ · Zhiliang Huang¹ · Jun Zhao¹ · E. Yang¹

Received: 5 December 2022 / Accepted: 25 August 2023 / Published online: 2 September 2023
© The Author(s), under exclusive licence to Springer-Verlag London Ltd., part of Springer Nature 2023

Abstract

The milling parameters have an important influence on machining performance and surface quality of metal materials. In this paper, the differences in machining and corrosion resistance properties of ZK61M plates under different processing parameters were analyzed by side milling. The milling process was simulated to explore the change laws of milling temperature and milling force. The hardness of machined surface was examined by Vickers hardness tester. The surface quality and the corrosion performances under different spindle speeds were observed by 3D ultra-depth of field microscope. The results showed that the milling temperature was increased as spindle speed and feed speed increased. The influence of spindle speed and feed speed on milling force along the milling direction and the tool direction was significant different. The milled surface had better quality when the spindle speed increased or the feed speed decreased. The hardness standard deviation of machined surface was decreased as the surface quality became better. Besides, it was summarized how spindle speed played a role in corrosion resistance performance by affecting residual stress and metal oxides.

Keywords Side milling · ZK61M magnesium alloy · Surface quality · Corrosion resistance properties

1 Introduction

Magnesium alloys have great potential applications in aerospace, automobile and defense fields due to their excellent physical properties such as low density and high strength [1–3]. As the numerical control technology develops and the milling process accuracy is improved, the magnesium alloy parts processed by milling are gradually widely used in manufacturing industry [4, 5].

At present, there are many researches on metal milling process. Umamaheswarrao et al. [6] studied the influence of processing parameters in end milling, and observed feed rate was most significant parameter affecting the responses followed by depth of cut, weight fraction, and speed. It was investigated that the cutting force coefficient had a nonlinear relationship with the feed per tooth and the spindle speed by means of the nonlinear instantaneous milling force [7]. An optimization model for cutting force was established to optimize the cutting parameters of plunge milling process

[8]. Benjamin et al. [9] designed a hybrid system that could separate chips more easily and increase the tool life through a decrease in cutting temperature and cutting force on the workpiece. The sensitive factors affecting surface topography and workpiece temperature were defined, and the research indicated that workpiece temperature grew up as the cutting velocity and maximum depth of cut increased [10]. Zhang et al. [11] observed the phase transformation reactions occurred in aluminum alloy during mechanical milling and discovered that mechanical milling was comprised of the same phases. Lu et al. [12] studied the effects of cutting parameters on Vickers hardness and built a Vickers hardness model to predict the micro-hardness based on a response surface methodology for milling Inconel718. Besides, some scholars had investigated the effect of process parameters on machining quality and evaluated the weight of influencing factors by mathematical method [13–15].

So far, the machining properties of magnesium alloys have been studied by some researchers. Adhikari et al. [16] investigated the influence of spindle speed, tangential feed, and axial pitch on milling force and microhardness during the helical hole milling process and summarized the machining characteristics of AZ31 magnesium alloy. Gobivel et al. [17] studied the influence of cutting

✉ Chenguang Wang
xinzewang618@163.com

¹ School of Mechanical and Electrical Engineering, Hunan City University, Yiyang 413002, China

parameters on end milling with AZ31B magnesium alloy and pointed out that the chip quality was adversely affected by feed rate. A comparative investigation on processing hole by conventional drilling and helical milling was made to demonstrate the advantages of helical hole milling [18]. Sivashankar et al. [19] analyzed the performance characteristics of Mg AZ61 alloy under different drill diameters and pointed out that the drill diameter was a significant parameter to minimize the overcut and improve the surface roughness. Chen et al. [20] applied a multi-objective optimization method to accurately predict the lowest residual stress level and pointed out that the cutting temperature was the crucial factor to affect the generation of the residual stress in Mg-Li Alloy milling process. Some scholars have analyzed the integrity of magnesium alloy processing interface and improved the processing surface through processing parameters. Pu et al. [21] explored the influence of different cutting-edge radius tools on surface integrity and discovered that cryogenic machining could enhance the surface integrity. Chen et al. [22] explored the effect of milled surface topography and texture direction on fatigue behavior of ZK61M magnesium alloy and discovered the workpiece with surface texture direction parallel to the fatigue loading direction had the largest fatigue life.

Magnesium alloys are widely used in industry, such as engine block of automobile parts, notebook computer shell, aircraft fuselage, and ship parts. However, magnesium alloy is relatively poor in corrosion resistance due to the complex working environment and active chemical properties. It has become a challenge which limits the application of magnesium alloy parts in industry. The corrosion behaviors of magnesium alloy and the microstructures were elucidated by some researches. They pointed out that the processing method and microstructure had influence on corrosion resistance [23–25].

As a kind of magnesium alloy, ZK61M magnesium alloy has higher specific strength and better machining performance. However, there are still some deficiencies in the research on milling performance of ZK61M magnesium alloy. The effect of processing parameters on milling quality has not been interpreted. The law about hardness

variation of magnesium alloy after milling has not been summarized.

In this paper, the milling samples of ZK61M magnesium alloy under different spindle speeds and feed speeds were observed to explore the effect of different parameters on surface quality. The numerical simulations were carried out to analyze the temperature and force in the milling process. Moreover, the mechanism was elaborated which the processed samples had different hardness values under different milling parameters. The reason for differences in machined surface topography of magnesium alloy samples under different spindle speeds was interpreted after neutral salt spray tests.

2 Materials and experimental steps

ZK61M magnesium alloy sheets were used in the milling experiments which the length, width, and thickness were 40 mm, 40 mm, and 3 mm respectively. The chemical compositions of ZK61M magnesium alloy sheets are listed in Table 1. Table 2 shows the mechanical properties of ZK61M magnesium alloy sheets.

The preparation process of the milled specimen is shown in Fig. 1. As shown in Fig. 1a, the milling experiments adopted a 5-axis high-speed machining center (JDGR400T) which could realize high-speed milling steadily. Figure 1b was the cemented carbide milling tools. The geometric and the property parameters of the milling tool are listed in Table 3 and Table 4. Figure 1c shows the assembly relationship of the milling process. The ZK61M magnesium alloy sheet was fixed on the clamp which was fastened on the machining center by the guide rail. The size of clamping part of ZK61M magnesium alloy was 40 mm × 20 mm. The workpieces were processed by down milling and the milling height of workpiece was 5 mm. The geometric dimensions of the sample after milling are shown in Fig. 1d.

Table 5 lists the processing parameters in milling experiments of ZK61M magnesium alloy sheet. The depth of milling was 1 mm in this series of experiment. Three samples were processed under each milling parameter condition

Table 1 Chemical composition of ZK61M magnesium alloy sheets (wt%) [26]

Zn	Zr	Mn	Fe	Si	Cu	Ni	Al	Mg
5.60	0.52	0.011	0.0027	0.0036	0.0011	0.0016	0.0012	Bal

Table 2 Mechanical properties of ZK61M magnesium alloy [27]

Material	Density (g/cm ³)	Poisson's ratio	Young's modulus (MPa)	Yield strength (MPa)	Specific heat capacity	Thermal conductivity (W/m·°C)
ZK61M	1.8	0.34	4480	285	0.2466	41.3

Fig. 1 The schematic of milling process: **a** the processing equipment. **b** The milling tools. **c** The assembly relationship of the milling process. **d** Geometric of the specimen

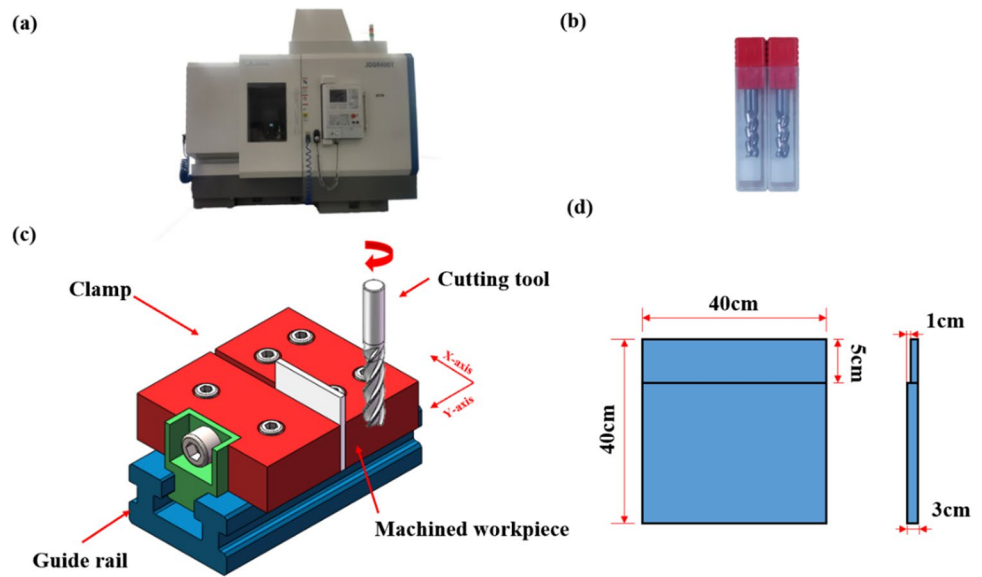


Table 3 Geometric parameters of cemented carbide milling tool

Diameter (mm)	Cutter length (mm)	Blade length (mm)	Rake angle (°)	Relief angle (°)	Helix angle (°)	Blade number (Z)
6	50	20	9	15	40	4

Table 4 The properties of the milling tool

Material	Young's modulus (MPa)	Poisson's ratio	Linear expansion coefficient (m/m.°C)	Specific heat capacity (J/Kg.°C)	Thermal conductivity (W/m-K)
YG8	6.4E+05	0.22	4.50E−06	220	7.54E+01

Table 5 The process parameters of the milling experiments

Experimental sample number	Spindle speed (r/min)	Feed speed (mm/min)	Number of repeated experiments
1	4000	3000	3
2	8000	3000	3
3	12,000	3000	3
4	4000	1000	3
5	8000	1000	3
6	12,000	1000	3

to ensure the accuracy of the experiments. The samples obtained by milling experiments are shown in Fig. 2.

The samples obtained by milling process are tested as shown in Fig. 3. In order to explore the influence of different milling parameters on machined quality, a 3D ultra-depth of field microscope (Smartzoom5) was used to observed microstructure of the samples (Fig. 3a). Then,

the hardness tests were performed by a Vickers hardness instrument as shown in Fig. 3b. Finally, neutral salt spray tests were carried out by Cyclic Corrosion Tester to explore the influence of different spindle speeds on corrosion results (Fig. 3c). Combining existing related research and the neutral salt spray test standard [28], this experiment selected the ISO 3768–1976 as reference.

3 Numerical simulation

3.1 The theory of 3D to 2D

Some numerical simulations had been conducted to explore the influence of milling parameters [29–31]. The cutting part of milling tool was generally approximate to cylindrical turning tool in the research about the cutting mechanism of milling process. Therefore, the turning principle was cited to analyze the milling process. At present, there are three main two-dimensional simplified models of milling process. As shown in Fig. 4, the simplified models included equivalent uniform cutting thickness model, workpiece slope cutting model, and workpiece oblique cutting model. The converted workpiece shape was described by the cutting length and the maximum undeformed shoulder thickness. The dimensions were calculated by the following formulas:

Fig. 2 The milled samples under different process parameters

Spindle speed \ Feed speed	4000rpm	8000rpm	12000rpm
3000 mm/min			
1000 mm/min			

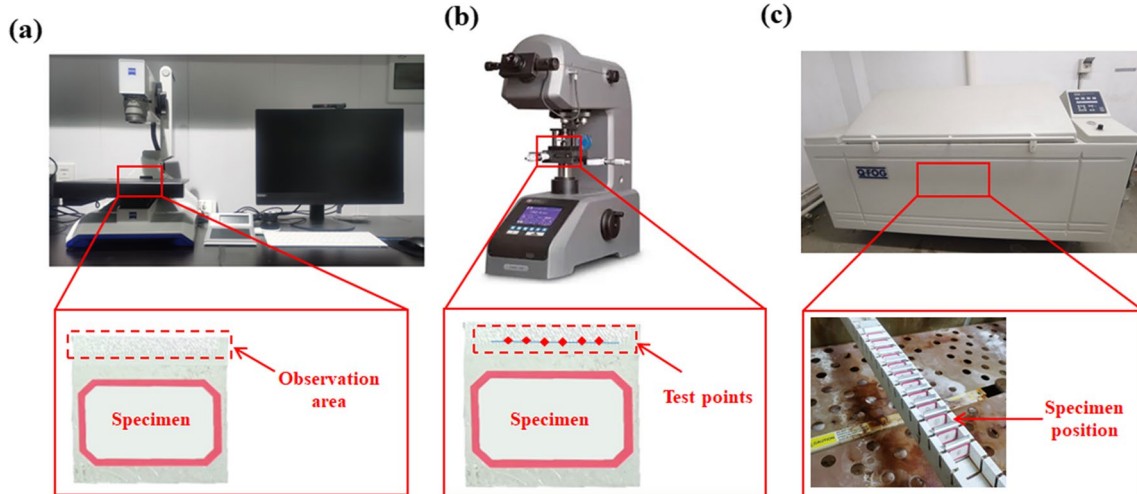
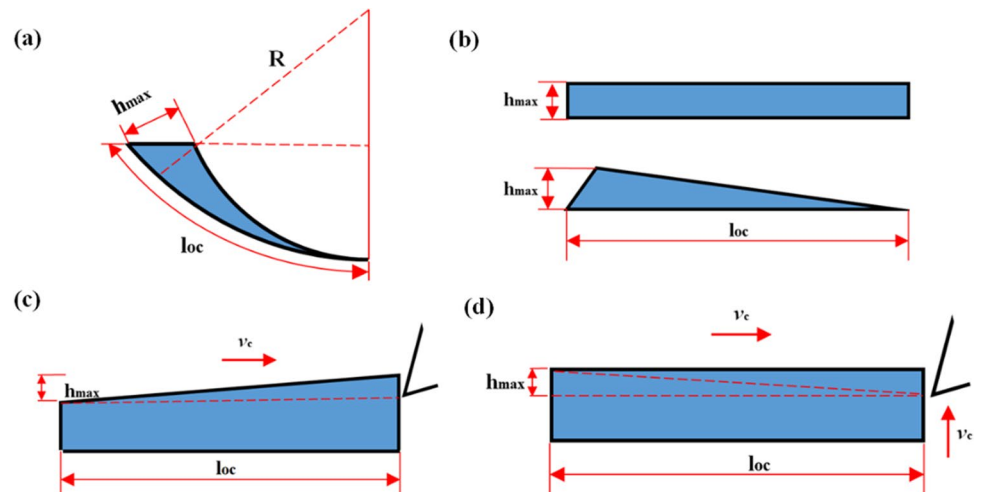


Fig. 3 The schematic of specimen tests: **a** microstructure observation; **b** hardness test; **c** neutral salt spray test

Fig. 4 Two-dimensional simplified milling models: **a** milling thickness; **b** equivalent uniform cutting thickness model; **c** slope cutting model; **d** oblique cutting model



$$l_{oc} = R \cdot \arccos\left(1 - \frac{a_e}{R}\right) \tag{1}$$

$$h_{max} = \frac{f_z \cdot \sqrt{2R \cdot a_e - a_e^2}}{R} \tag{2}$$

where l_{oc} is the cutting length, h_{max} is the maximum undeformed shoulder thickness, f_z is feed per tooth, a_e is cutting depth, and R is the milling tool radius.

As for cutting force, there was a conversion relationship between two-dimensional cutting force and three-dimensional cutting force. The cutting force F_x and F_y were in the measurement coordinate system. The cutting force F_r and F_c were in the two-dimensional cutting coordinate system. The conversion relation was obtained by following formula when the helix angle η of milling tool was 0° :

$$\begin{bmatrix} F_c \\ F_r \end{bmatrix} = \begin{bmatrix} \sin(\theta - wt) & -\cos(\theta - wt) \\ \cos(\theta - wt) & \sin(\theta - wt) \end{bmatrix} \begin{bmatrix} F_x \\ F_y \end{bmatrix} \tag{3}$$

where θ is entrance angle of milling tool and w is angular velocity of milling tool. When helix angle η of milling tool was not 0° , the original measuring coordinate system was rotated around the y -axis by η to establish the auxiliary coordinate system $o-\hat{x}\hat{y}\hat{z}$. In the auxiliary coordinate system, the relationship between dimensional cutting force and two-dimensional cutting force was described as follows:

$$\begin{bmatrix} \hat{F}_x \\ \hat{F}_y \\ \hat{F}_z \end{bmatrix} = \begin{bmatrix} \cos\eta\cos(\theta - wt - \gamma_n) & -\cos(\theta - wt) \\ \cos\eta\cos(\theta - wt - \gamma_n) & \sin(\theta - wt) \\ \sin\eta & 0 \end{bmatrix} \begin{bmatrix} \cos\gamma_n & \sin\gamma_n \\ -\sin\gamma_n & \cos\gamma_n \end{bmatrix} \begin{bmatrix} F_r \\ F_c \end{bmatrix} \tag{4}$$

The cutting force in the auxiliary coordinate system $o-\hat{x}\hat{y}\hat{z}$ was converted into the cutting force in the measuring coordinate system $o-xyz$ by following equation:

$$\begin{bmatrix} F_x \\ F_y \\ F_z \end{bmatrix} = \begin{bmatrix} \cos\eta & 0 & \sin\eta \\ 0 & 1 & 0 \\ -\sin\eta & 0 & \cos\eta \end{bmatrix} \begin{bmatrix} \hat{F}_x \\ \hat{F}_y \\ \hat{F}_z \end{bmatrix} \tag{5}$$

Then, the conversion between 3D cutting force and 2D cutting force was realized by the above conversion method.

3.2 The establishment of simulation model

The milling process was simulated by AdvantEdge FEM which was a professional CAE software for metallic material processing simulation. The Johnson–Cook (J-C) material model was used to analyze the fracture behavior of ZK61M magnesium alloy in the milling simulation, which could describe the mechanical properties accurately under high strain rates and high temperature. The flow stress

Table 6 The J-C material model parameters for ZK61M magnesium alloy [32]

Material	A (MPa)	B (MPa)	C	n	m
ZK61M	175	332	0.0198	0.448	1.47

Table 7 Converted down milling geometric parameters of simulation

Sample number	Radial width of cut (mm)	Axial depth of cut (mm)	Feed per tooth (mm)	l_{oc} (mm)	h_{max} (mm)
1	1	5	0.1875	2.523	0.13975
2	1	5	0.09375	2.523	0.069877
3	1	5	0.0625	2.523	0.04658
4	1	5	0.0625	2.523	0.04658
5	1	5	0.03125	2.523	0.023292
6	1	5	0.02083	2.523	0.0155

of the material model could be described by following formula:

$$\sigma = (A + B\epsilon^n) \left(1 + C \ln \frac{\dot{\epsilon}}{\epsilon_0} \right) [1 - T^{*m}] \tag{6}$$

where σ is the equivalent plastic stress, ϵ is the equivalent plastic strain, $\frac{\dot{\epsilon}}{\epsilon_0}$ is the equivalent plastic strain rate, $\frac{\dot{\epsilon}}{\epsilon_0}$ is the reference equivalent plastic strain rate, and T^* is the dimensionless temperature. A , B , C , m , and n are material parameters. The J-C material model parameters for ZK61M magnesium alloy are shown in Table 6. Compared with ZK61M magnesium alloy, the tool had a higher hardness and wear resistance. Therefore, the milling tool was considered as a rigid body when establishing the simulation model. Table 7 is the geometric parameters of ZK61M magnesium alloy in 2D milling simulation.

As for element separation criteria, we adopted Johnson–Cook shear failure physical separation model, which was suitable for the situation of high strain rate and high temperature deformation. According to the friction properties, the friction zone could be divided into two parts in the milling process. One was the bonding zone; the other was the sliding zone. The model equation based on Coulomb’s friction law for the friction stress was:

$$\begin{cases} T_f = \mu\sigma_n & (\mu\sigma_n < \bar{\tau}_s) \\ T_f = \bar{\tau}_s & (\mu\sigma_n \geq \bar{\tau}_s) \end{cases} \tag{7}$$

where T_f is friction stress, σ_n is normal stress, μ is friction coefficient, $\bar{\tau}_s$ is ultimate stress of material.

In order to improve the accuracy of the cutting force and temperature, The boundary conditions of the milling process were established by combining the physical parameters and motion conditions. Then, the differential equations of motion and heat transfer in the milling process are solved by Lagrange and Euler methods in the simulation software.

The schematic diagram of grid division during in milling process is shown in Fig. 5. The triangular mesh was adopted to the grid division of the milling tool and workpiece. The milling tool had 3156 grids, and the workpiece had 78,125 grids totally. For the milling tool, the maximum element size was 0.1 mm, and the minimum element size was 0.02 mm. For the ZK61M magnesium alloy sheet, the maximum and minimum element size was 0.05 mm and 0.002 mm, respectively. The adaptive mesh and mesh refinement technology were used to make the simulation results more similar to the actual milling process.

4 Results and discussion

4.1 Simulation model verification

To ensure the accuracy of the simulation model, a force-measuring system was established to measure the milling force when the spindle speed was 4000 rpm and feed speed was 3000 mm/min. As shown in Fig. 6a, the system was composed of the dynamometer, charge amplifier data acquisition device. Figure 6b is the main components of force-measuring system. Then, the data was processed and analyzed by the computer software, and the milling force in the experiment was measured finally.

Figure 7a shows the original signal from the force-measuring system. The calculated milling force in the simulation and the measured force from the experimental platform are compared in Fig. 7b. When the spindle speed was 4000 rpm and feed speed was 3000 mm/min, the calculated maximum forces along x -axis and y -axis were 723.7 N and 128.3 N in the simulation. The measured maximum forces along x -axis

Fig. 5 The establishment of two-dimensional simulation model

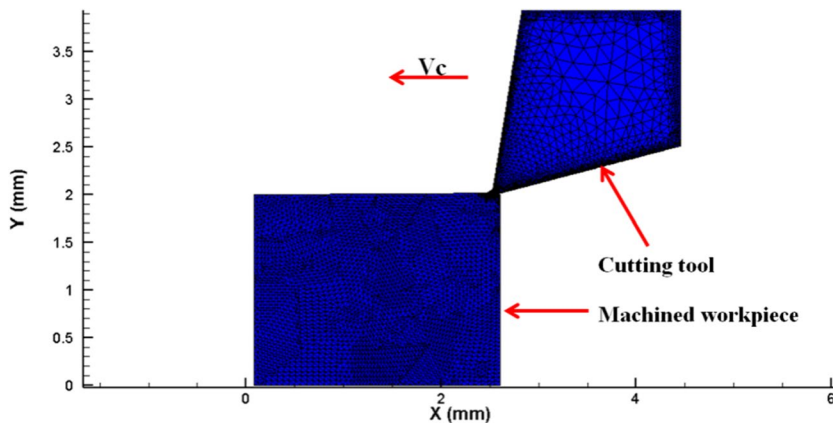


Fig. 6 The force-measuring system: **a** sketch of experimental platform for force measurement; **b** the main components of the system

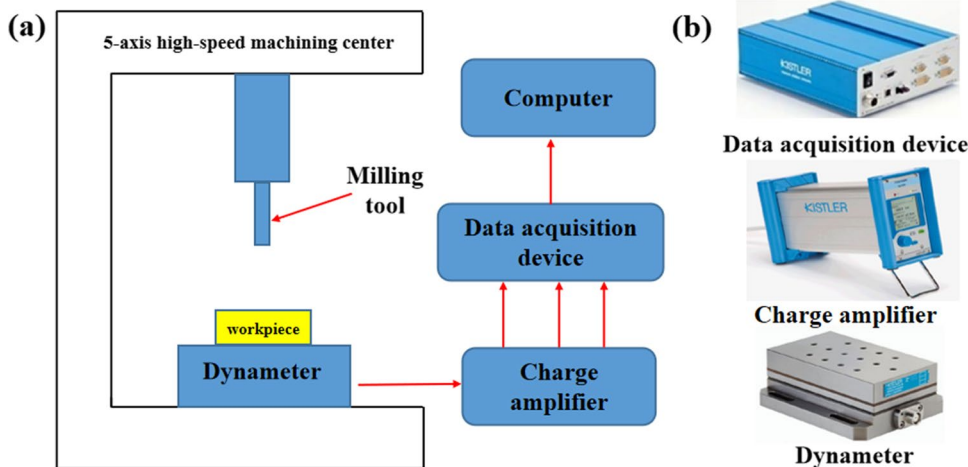
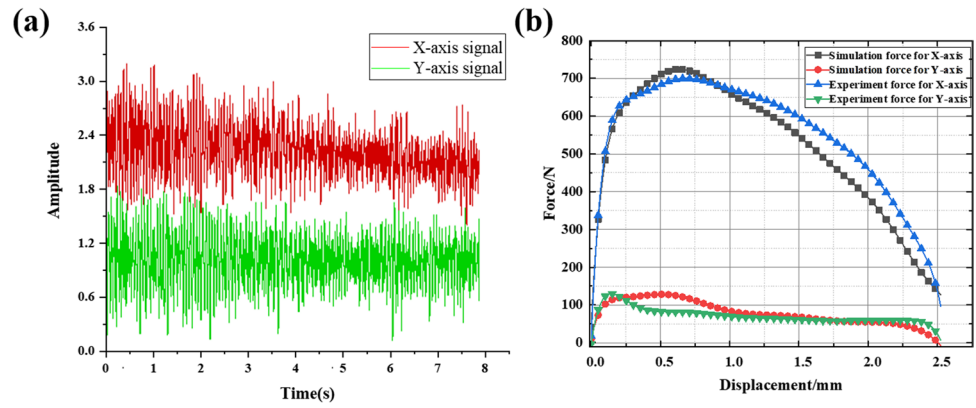


Fig. 7 Experiment and simulation comparison: **a** the original signal in the experiment; **b** force curves in experiment and simulation



and y-axis were 699.8 N and 129.7 N. The relative errors of the maximum force along x-axis and y-axis between simulation and experiment were 3.42% and 1.08%, respectively. The simulation results were in good agreement with the experimental results.

4.2 Simulation result analysis

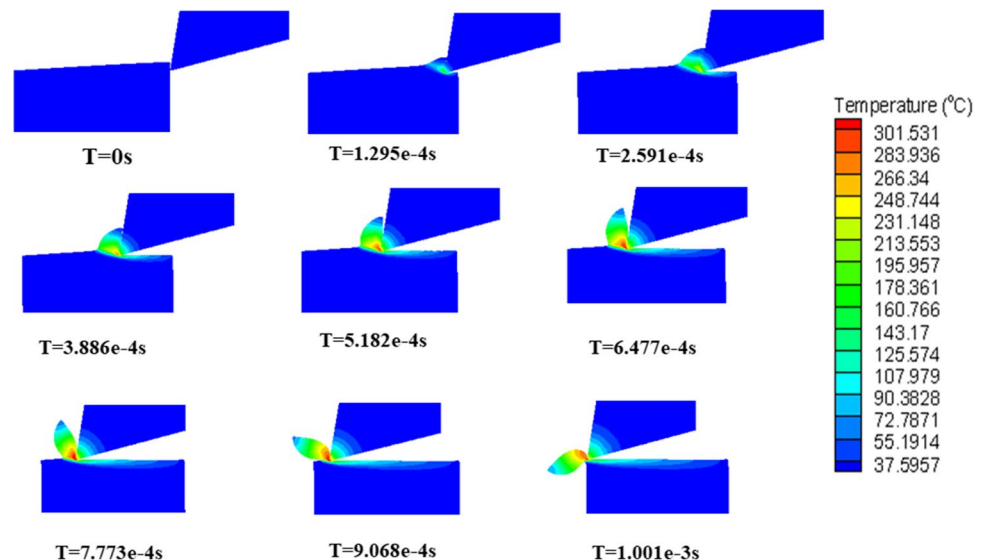
Figure 8 shows the temperature change of ZK61M magnesium alloy in milling process simulation (taking the processing parameters of specimen 1 as an example). It was discovered that the temperature increased gradually in the simulation as the milling time increased. When the cutting was fully realized, the temperature of workpiece and tool reached the maximum value. Besides, it could be found that the heat generated in the cutting process was mainly concentrated in the cut tool blade, the chips, and the machined surface.

The differences in cutting temperature under different spindle speeds and feed speeds are shown in Fig. 9. When the feed speed was 3000 mm/min and spindle speed of cutter

increased from 4000 to 12000 rpm, the maximum milling temperature was also increased (from about 301.5 to 321.4 °C and 334.7 °C). When the feed speed was 1000 mm/min, the maximum milling temperature was increased from 220.1 to 264.6 °C and 298.1 °C with the spindle speed increased from 4000 to 8000 rpm and 12,000 rpm. As the spindle speed increased, the energy cutting tool transmitted to the workpiece increased. Then, the internal energy increased which would cause a higher maximum temperature. When the feed speed increased, the length of material cut by the tool in unit time which would make the cutting heat increase and the maximum temperature go up. Hence, the maximum temperature in milling process was increased as the spindle speed was the same and the feed speed increased.

The milling forces in the milling process under different parameters are shown in Fig. 10. At the beginning, the milling force increased sharply with the increased cutting area because the milling force needed to grow up to meet the fracture requirements of ZK61M magnesium alloy material. Meanwhile, the large amount of heat generated in the milling

Fig. 8 The simulation of ZK61M magnesium alloy cutting process



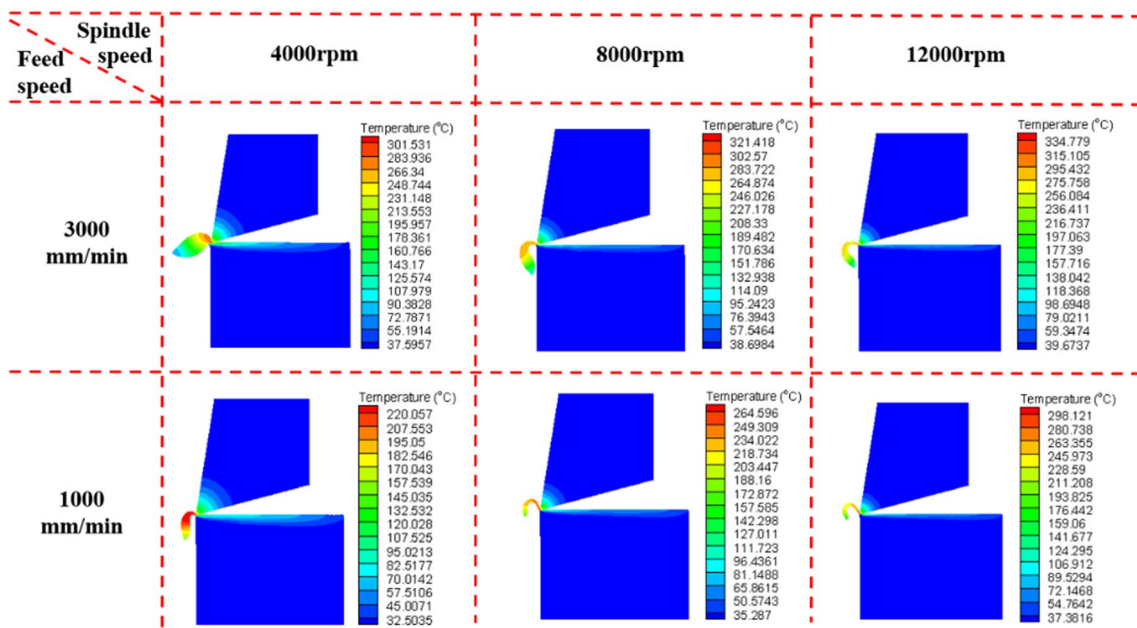
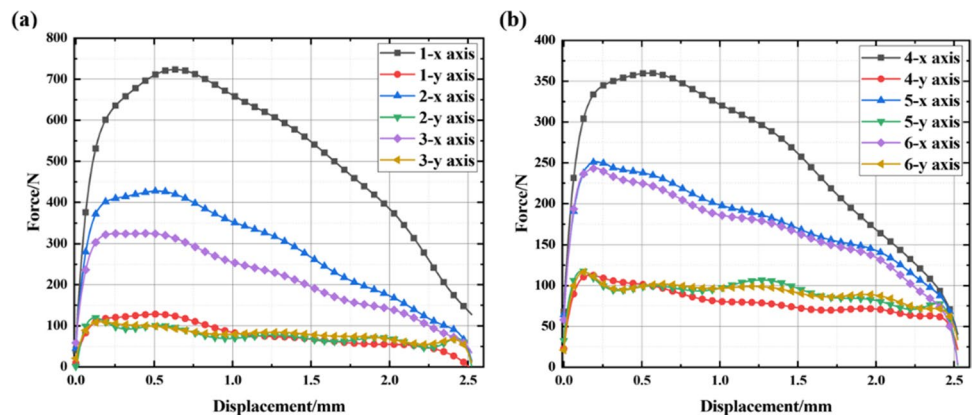


Fig. 9 The maximum milling temperature under different parameters

process would make the temperature rise and decrease the deformation resistance of material which led to a gradual increase in milling force until reaching the maximum value. Then, the heat was further accumulated, and the temperature was further increased which would cause the plastic deformation of the ZK61M material and make the milling force reduce gradually. It could be discovered that there were differences in milling force at *x*-axis direction (the cutting direction) and *y*-axis direction (the cutter direction) as shown in Fig. 10. One possible reason for this phenomenon: the milling heat mainly accumulated along the *x*-axis direction. While the milling force on *y*-axis direction was mainly affected by the tool pressure, the cutting heat accumulation was less. Therefore, the temperature variation in *x*-axis direction was larger than that in *y*-axis direction, which would cause milling force at the *y* axis change to be more stable.

Figure 11 shows the maximum force in milling process under different experimental parameters. When the feed speed was the same, the milling temperature was increased with the spindle speed increased from 4000 to 8000 rpm and 12,000 rpm, which would make the plastic deformation of ZK61M material increase. As a result, the maximum force in *x*-axis direction was decreased as the spindle speed increased. When the spindle speed was the same and the feed speed increased, the cutting length increased in unit time, and the cutting material thickness of each blade also increased. Therefore, the maximum force in *x*-axis direction was increased when the feed speed increased from 1000 to 3000 mm/min. The cutting heat was mainly accumulated along *x*-axis direction, and the cutting heat transferred along *y*-axis direction had little effect on the temperature change of ZK61M material. The force in *y*-axis direction was mainly

Fig. 10 The force in milling process: **a** feed speed 3000 mm/min, spindle speed 4000 rpm, 8000 rpm, and 12,000 rpm; **b** feed speed 1000 mm/min, spindle speed 4000 rpm, 8000 rpm, and 12,000 rpm



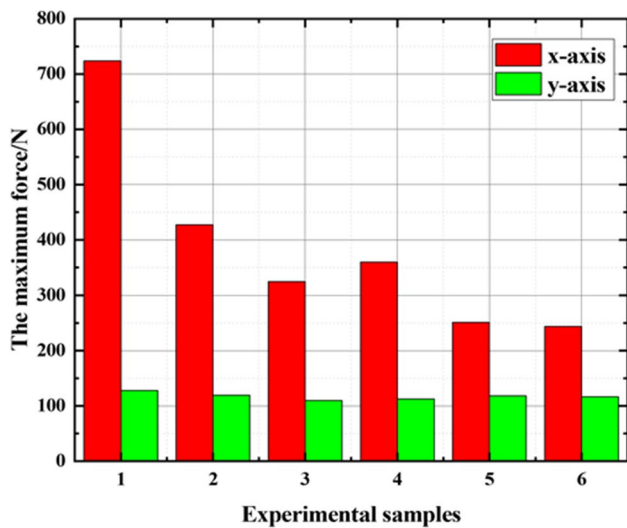


Fig. 11 The maximum force under different parameters in milling simulation

dominant by the tool pressure. Hence, the change of the maximum force in y-axis direction was small, and the fluctuation was maintained at the range of 100–130 N when the feed speed and spindle speed were different.

4.3 Experimental results and analysis

The microhardness measurement results under different spindle speeds and feed speeds are shown in Table 8. In order to explore the relationship between specimen microhardness more intuitively, the average value, extreme difference, and the standard deviation of hardness values for each specimen were calculated. Figure 12 shows the difference of Vickers hardness on machined surface of each specimen.

The hardness after milling was related to the plastic deformation and temperature of the metal in the milling process. The hardness of machined surface was increased when the milled surface deformation increased. However, the hardness of the machined surface decreased when the temperature in the milling process went up [33, 34]. When

the feed speed was the same but the spindle speed was different, the milling temperature played a major role in the hardness of the machined surface. Therefore, the specimen hardness value was gradually decreased as the spindle speed increased from 4000 to 8000 rpm and 12,000 rpm due to the increased temperature. The standard deviation of specimen hardness also decreased which meant the hardness value of the milled surface was more concentrated towards the average value, and the quality of the milled surface was higher. When the spindle speed was the same, the deformation of processed material was the main influencing factor of specimen hardness, and the deformation increased with the increased feed speed. As a result, the Vickers hardness, the average value, extreme difference, and standard deviation of the material milled surface decreased when the feed speed decreased gradually.

In the side milling process, the texture structure would be formed on the machined surface because the metal material was removed intermittently by rotation of each

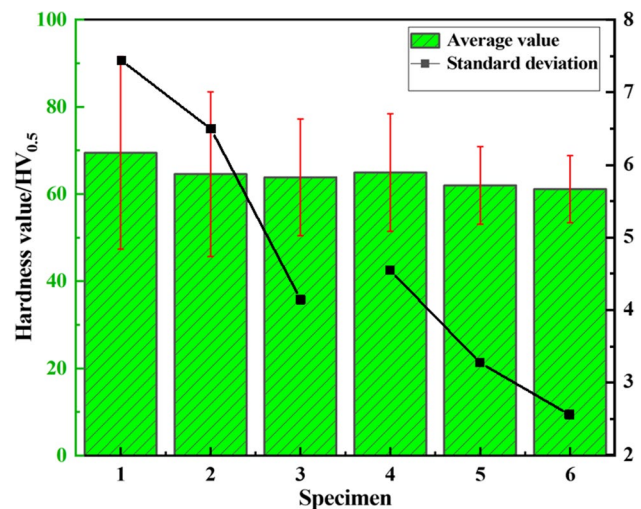


Fig. 12 The hardness value of specimen under different experimental parameters

Table 8 Vickers hardness value of milled surface for different specimens

Specimen	1	2	3	4	5	6
	67.9	70	63.3	71.5	61.8	61
	75.6	61.1	67	68.9	66	60.6
	64.9	75.2	61.8	62.2	59.7	61.9
	82.3	64.7	64.3	66.6	61.2	63.7
	65.4	62.4	70	64.9	60.8	61
	75.1	69.1	66.6	67.2	68	65.1
Average value	69.45	64.5625	63.8375	64.9375	61.9875	61.1125
Extreme difference	22.1	18.9	13.4	13.5	8.9	7.7
Standard deviation	7.4402	6.4956	4.1427	4.5468	3.2756	2.5570

blade in tool. There were differences on texture structure and surface quality when milling parameters were different. As illustrated in Fig. 13, the surface morphology after milling was observed under different processing parameters. There were troughs and ridges on the milled surface. The surface topography quality was related to the feed rate of each tooth. When the feed rate of each tooth was large, obvious troughs and ridges were formed on the machined surface during milling, and the consistency was poor. When the feed speed was decreased, the feed rate of each tooth decreased. The troughs and the ridges became less obvious and the quality of milled surface became better. When feed speed was the same, the milling length in feed direction decreased with the increase of spindle speed when each blade finished milling. Then, the extrusion deformation between two adjacent blades became smaller, which had a great advantage on improving the milled surface quality. Hence, the troughs and ridges on machined surface become more and more regular as the spindle speed increased. Besides, the milled surface roughness was reduced by degrees with the increased spindle speed.

The metal milling process was essentially a process the workpiece was squeezed and rubbed by the tool, which resulted in elastic deformation and plastic deformation on the workpiece surface, then the chip was separated from the parent body. The residual stress was generated in machined material under the interaction of deformation, mechanical stress, and thermal stress. The residual stress had an important influence on the fatigue resistance and corrosion resistance of the workpiece [35].

Figure 14 shows the salt spray corrosion on the machined surface at the feed speed of 1000 mm/min and the spindle speed of 4000 rpm, 8000 rpm, and 12,000 rpm. From Fig. 14, there were differences in the corrosion of the milled surface with different spindle speeds. When the corrosion time was 1 h, cracks appeared on the surface topography. Besides, corrosion pits were generated on the machined surface when the corrosion time increased to 8 h.

The spindle speed further affected the corrosion of the machined metal material surface by influencing residual stress. On the one hand, when the feed speed was the same, the milling amount of each blade in tool was decreased as the spindle speed increased. The deformation of the material was reduced and the residual stress was decreased. On the other hand, the milling temperature was increased with the increase of spindle speed which would also reduce the residual stress. The salt corrosion process was accompanied by the slow release of the residual stress on the machined surface. Therefore, corrosion cracks would form on the machined material surface. As shown in Fig. 14a, the cracks were relatively obvious and extended around due to the release of large residual stress with the spindle speed of 4000 rpm. When the spindle speed was 8000 rpm, the crack morphology was relatively slender and had obvious directivity because of reduced residual stress. As the spindle speed increased to 12,000 rpm, the residual stress further reduced which resulted in smaller cracks on the machined surface with corrosion spots.

The workpiece would produce oxide layer on the machined surface during milling process, and the

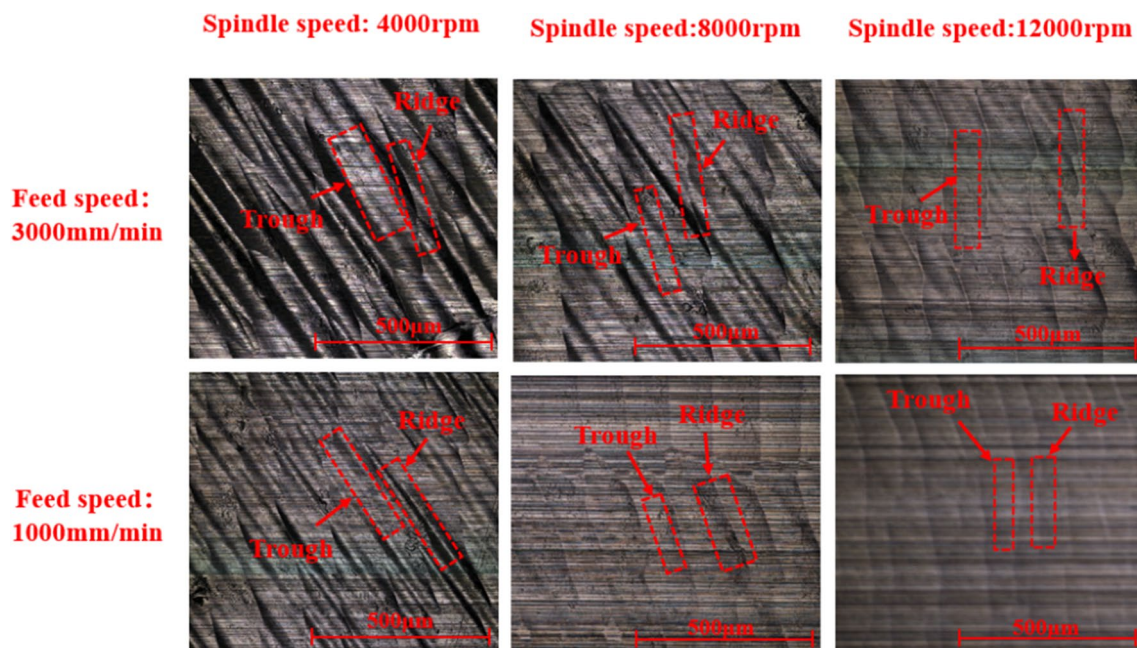


Fig. 13 The surface morphology under different milling parameters

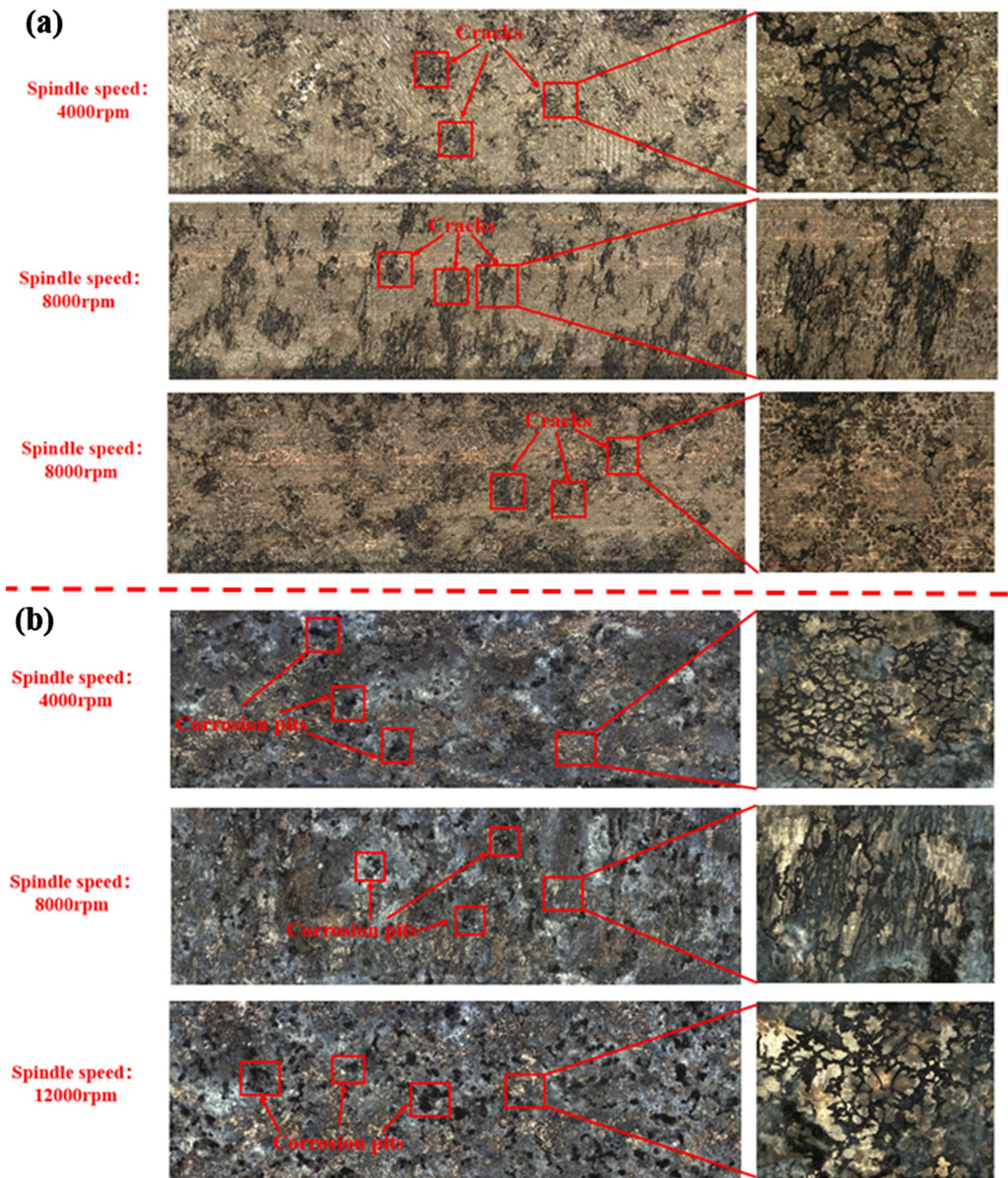


Fig. 14 The salt spray corrosion result: **a** corrosion time: 1 h; **b** corrosion time: 8 h

formation of intermetallic oxides increased with the increase of temperature [36]. The corrosion resistance of magnesium alloys was related to intermetallic oxides and decreased with the increased surface oxides. When

the corrosion time increased and the residual stress was gradually released, the oxides on machined surface played a major role in salt spray corrosion. In this experiment, the milling temperature increased with the increased spindle

speed, resulting in the gradual increase of oxides formed on the machined surface. Therefore, the number of corrosion pits increased with the spindle speed from 4000 rpm, 8000 rpm, and 12,000 rpm as shown in Fig. 14b when the corrosion time reached 8 h.

5 Conclusions

In this paper, the effects of different milling parameters on machined properties and corrosion performances for ZK61M magnesium alloy were investigated. Based on the above analysis and results, the following conclusions could be drawn:

1. The milling temperature was related to the spindle speed and feed speed in ZK61M magnesium alloy milling process. When the spindle speed increased from 4000, 8000 to 12,000 rpm, the milling temperature increased gradually. The milling temperature also increased as the feed speed increased.

2. There were differences in the milling force at x -axis and y -axis direction. The maximum value of milling force was increased with the increased of feed speed but decreased with the increase of spindle speed. The change of milling parameters had little influence on milling force at y -axis direction and the change of milling force was more stable compared with the milling force at x -axis direction.

3. When the spindle speed increased or the feed speed decreased, the hardness value of machined surface was increased. The quality of the milled surface was better with a higher spindle speed and a smaller feed speed. Besides, the standard deviation of hardness was relatively small when the machined surface quality was superior.

4. The spindle speed had influence on the corrosion performance by affecting the residual stress and the formation of metal oxides on machined surface in ZK61M magnesium alloy milling process. At the beginning, the corrosion cracks were gradually slender with the increase of spindle speed. As corrosion time increased, the number of corrosion pits was increased due to the increased temperature and surface oxides when the spindle speed increased.

Author contribution Chenguang Wang: conceptualization, formal analysis, writing—original draft, and writing—review and editing.

Chang Chen: software, writing—review and editing, and visualization.

Jun Zhao: investigation, resources, and project administration.

E. Yang: preparation and investigation.

Zhiliang Huang: validation, supervision, writing—review and editing, and project administration.

Funding This project is supported by the Scientific Research Project of Hunan Education Department (21B0726), the Natural Science

Foundation of Hunan Province (2021JJ30077), the Research Project of Teaching Reform for Colleges and Universities in Hunan Province (HNJG-2021–0872), and the Cooperative Education Project of Higher Education Department of Ministry of Education (202102046031).

Data availability The raw/processed data required which reproduce these findings cannot be shared at this time due to technical or time limitations.

Declarations

Conflict of interest The authors declare no competing interests.

References

1. Carou D, Rubio EM, Lauro CH, Davim JP (2016) The effect of minimum quantity lubrication in the intermittent turning of magnesium based on vibration signals. *Measurement* 94:338–343. <https://doi.org/10.1016/j.measurement.2016.08.016>
2. Mirzadeh H (2014) Constitutive analysis of Mg–Al–Zn magnesium alloys during hot deformation. *Mech Mater* 77(5):80–85
3. Wang LX, Fang G, Leeflang MA, Zhou J (2015) Constitutive behavior and microstructure evolution of the as-extruded AE21 magnesium alloy during hot compression testing. *J Alloy Compd* 622(5):121–129
4. Ulacia I, Salisbury CP, Hurtado I, Worswick MJ (2011) Tensile characterization and constitutive modeling of AZ31B magnesium alloy sheet over wide range of strain rates and temperatures. *J Mater Process Tech* 211(5):830–839
5. Kulekci MK (2008) Magnesium and its alloys applications in automotive industry. *Int J Adv Manuf Tech* 39:851–865. <https://doi.org/10.1007/s00170-007-1279-2>
6. Umamaheswarrao P, Sankar BR, Nanchaiah T (2020) Multi objective optimization of process parameters of Al 6061–SiCp metal matrix composite in end milling-Hybrid GRA-PCA approach. *Mater Today: Proc* 26(2):696–700. <https://doi.org/10.1016/j.matpr.2019.12.407>
7. Zhai YS, Gao HN, Wang Y, Li RY (2019) Influence of cutting parameters on force coefficients and stability in plunge milling. *Int J Adv Manuf Tech* 104:2513–2523. <https://doi.org/10.1007/s00170-019-04036-y>
8. Zhuang KJ, Zhang XM, Zhang D, Ding H (2013) On cutting parameters selection for plunge milling of heat-resistant-super-alloys based on precise cutting geometry. *J Mater Process Tech* 213(8):1378–1386. <https://doi.org/10.1016/j.jmatprotec.2013.03.007>
9. Benjamin DM, Sabarish VN, Hariharan MV, Raj DS (2018) On the benefits of sub-zero air supplemented minimum quantity lubrication systems: an experimental and mechanistic investigation on end milling of Ti-6-Al-4-V alloy. *Tribol Int* 119:464–473. <https://doi.org/10.1016/j.triboint.2017.11.021>
10. Liu C, He Y, Wang YL, Li YF, Wang SL, Wang LX, Wang Y (2019) An investigation of surface topography and workpiece temperature in whirling milling machining. *Int J Mech Sci* 164:105182. <https://doi.org/10.1016/j.ijmecsci.2019.105182>
11. Zhang ZH, Zhou YZ, Lavernia EJ (2008) Amorphization and crystallization in Al–Ni–La during mechanical milling. *J Alloy Compd* 466(1–2):189–200. <https://doi.org/10.1016/j.jallcom.2007.11.107>
12. Lu XH, Jia ZY, Wang H, Feng YX, Liang SY (2019) The effect of cutting parameters on micro-hardness and the prediction of Vickers hardness based on a response surface methodology for micro-milling Inconel 718. *Measurement* 140:56–62. <https://doi.org/10.1016/j.measurement.2019.03.037>

13. Kawin N, Jagadeesh D, Saravanan G, Periasamy K (2020) Optimization of turning parameters in sugarcane bagasse ash reinforced with Al-Si10-Mg alloy composites by Taguchi method. *Mater Today: Proc* 21(1):474–476. <https://doi.org/10.1016/j.matpr.2019.06.634>
14. Viswanathan R, Ramesh S, Maniraj S, Subburam V (2020) Measurement and multi-response optimization of turning parameters for magnesium alloy using hybrid combination of Taguchi-GRAPCA technique. *Measurement* 159:107800. <https://doi.org/10.1016/j.measurement.2020.107800>
15. Shi KN, Zhang DH, Ren JX (2015) Optimization of process parameters for surface roughness and microhardness in dry milling of magnesium alloy using Taguchi with grey relational analysis. *Int J Adv Manuf Tech* 81:645–651. <https://doi.org/10.1007/s00170-015-7218-8>
16. Adhikari R, Bolar G, Shanmugam R, Koklu U (2023) Machinability and surface integrity investigation during helical hole milling in AZ31 magnesium alloy. *Int J Lightweight Mater Manuf* 6(2):149–164. <https://doi.org/10.1016/j.ijlmm.2022.09.006>
17. Gobivel K, Vijay Sekar KS (2022) Influence of cutting parameters on end milling of magnesium alloy AZ31B. *Mater Today: Proc* 62(2):933–937. <https://doi.org/10.1016/j.matpr.2022.04.075>
18. Gonsalves JA, Nayak SN, Bolar G (2022) Experimental investigation on the performance of helical milling for hole processing in AZ31 magnesium alloy. *J King Saud Univ Eng Sci* 34(5):366–374. <https://doi.org/10.1016/j.jksues.2020.10.004>
19. Sivashankar N, Viswanathan R, Periasamy K, Venkatesh R, Chandrakumar S (2021) Multi-objective optimization of performance characteristics in drilling of Mg AZ61 using twist end mill drill tool. *Mater Today: Proc* 37(2):214–219. <https://doi.org/10.1016/j.matpr.2020.05.033>
20. Chen ZJ, Qian LY, Cui RK, Liu JS, Zhang QD (2022) Machining-induced residual stress analysis and multi-objective optimization for milling process of Mg–Li alloy. *Measurement* 204:112127. <https://doi.org/10.1016/j.measurement.2022.112127>
21. Pu Z, Outeiro JC, Batista AC, Dillon OW, Puleo DA, Jawahir IS (2012) Enhanced surface integrity of AZ31B Mg alloy by cryogenic machining towards improved functional performance of machined components. *Int J Mach Tool Manu* 56:17–27. <https://doi.org/10.1016/j.ijmactools.2011.12.006>
22. Chen SQ, Zhao WX, Yan P, Qiu TY, Gu HQ, Jiao L, Wang XB (2022) Effect of milling surface topography and texture direction on fatigue behavior of ZK61M magnesium alloy. *Int J Fatigue* 156:106669. <https://doi.org/10.1016/j.ijfatigue.2021.106669>
23. Esmaily M, Svensson JE, Fajardo S, Birbilis N, Frankel GS, Virtanen S, Arrabal R, Thomas S, Johansson LG (2017) Fundamentals and advances in magnesium alloy corrosion. *Prog Mater Sci* 89:92–193
24. Naik GM, Narendranath S, Kumar SSS (2019) Effect of ECAP die angles on microstructure mechanical properties and corrosion behavior of AZ80 Mg alloy. *J Mater Eng Perform* 28:2610–2619
25. Yang ZQ, Ma AB, Xu BQ, Jiang JH, Sun JP (2021) Corrosion behavior of AZ91 Mg alloy with a heterogeneous structure produced by ECAP. *Corros Sci* 187:109517. <https://doi.org/10.1016/j.corsci.2021.109517>
26. Yang L, Duan YC, Guan YP (2023) Ductile fracture prediction of ZK61M high-strength magnesium alloy sheet during hot deformation process. *Trans Nonferrous Met Soc China* 33(1):95–106. [https://doi.org/10.1016/S1003-6326\(22\)66093-X](https://doi.org/10.1016/S1003-6326(22)66093-X)
27. Chen XL, Xu CG, Jin H, Qin SX (2020) Hot compression deformation behavior of extruded ZK61M magnesium alloy and establishment of constitutive equation. *Procedia Manuf* 50:637–641. <https://doi.org/10.1016/j.promfg.2020.08.114>
28. Xia M, Wang YD, Xu SH (2021) Study on surface characteristics and stochastic model of corroded steel in neutral salt spray environment. *Constr Build Mater* 272:121915. <https://doi.org/10.1016/j.conbuildmat.2020.121915>
29. Afazov SM, Ratchev SM, Segal J (2010) Modelling and simulation of micro-milling cutting forces. *J Mater Process Tech* 210(15):2154–2162. <https://doi.org/10.1016/j.jmatprotec.2010.07.033>
30. Zhang P, Xiujie Y, Han SF, Song AL, Li BS, Yu X (2020) Experiment and simulation on the high-speed milling mechanism of aluminum alloy 7050–T7451. *Vacuum* 182:109778. <https://doi.org/10.1016/j.vacuum.2020.109778>
31. Danis I, Monies F, Lagarrigue P, Wojtowicz N (2016) Cutting forces and their modelling in plunge milling of magnesium-rare earth alloys. *Int J Adv Manuf Tech* 84:1801–1820. <https://doi.org/10.1007/s00170-015-7826-3>
32. Deng YF, Hu A, Xiao XK, Jia B (2021) Experimental and numerical investigation on the ballistic resistance of ZK61m magnesium alloy plates struck by blunt and ogival projectiles. *Int J Impact Eng* 158:104021. <https://doi.org/10.1016/j.ijimpeng.2021.104021>
33. Rotpai U, Arlai T, Nusen S, Juijerm P (2022) Novel flow stress prediction and work hardening behavior of aluminium alloy AA7075 at room and elevated temperatures. *J Alloy Compd* 891:162013. <https://doi.org/10.1016/j.jallcom.2021.162013>
34. Fu YJ, Cheng Y, Cui Y, Xin YC, Shi SW, Chen G (2022) Deformation mechanisms and differential work hardening behavior of AZ31 magnesium alloy during biaxial deformation. *J Magnes Alloy* 10(2):478–491. <https://doi.org/10.1016/j.jma.2020.09.022>
35. Qi FZ, Zhang XL, Wu GH, Liu WC, Wen L, Xie H, Xu SH, Tong X (2022) Effect of heat treatment on the stress corrosion cracking behavior of cast Mg-3Nd-3Gd-0.2Zn-0.5Zr alloy in a 3.5 wt% NaCl salt spray environment. *Mater Charact* 183:111630. <https://doi.org/10.1016/j.matchar.2021.111630>
36. Manivannan S, Dinesh P, Babu KSP, Sundarajan S (2015) Investigation and corrosion performance of cast Mg–6Al–1Zn + XCa alloy under salt spray test (ASTM-B117). *J Magnes Alloy* 3(1):86–94. <https://doi.org/10.1016/j.jma.2015.02.002>

Publisher's Note Springer Nature remains neutral with regard to jurisdictional claims in published maps and institutional affiliations.

Springer Nature or its licensor (e.g. a society or other partner) holds exclusive rights to this article under a publishing agreement with the author(s) or other rightsholder(s); author self-archiving of the accepted manuscript version of this article is solely governed by the terms of such publishing agreement and applicable law.